Magnetic structure and spin reorientation of quaternary $Dy_2Fe_2Si_2C$

2017 J. Phys.: Condens. Matter 29 115806

(http://iopscience.iop.org/0953-8984/29/11/115806)

IOP Publishing Journal of Physics: Condensed Matter

J. Phys.: Condens. Matter **29** (2017) 115806 (9pp) doi:10.1088/1361-648X/aa52f9

Magnetic structure and spin reorientation of quaternary $Dy_2Fe_2Si_2C$

R A Susilo[1], J M Cadogan[1], W D Hutchison[1], G A Stewart[1], M Avdeev[2,3] and S J Campbell[1]

[1] School of Physical, Environmental and Mathematical Sciences, UNSW Canberra at the Australian Defence Force Academy, Canberra BC 2610, Australia
[2] Australian Centre for Neutron Scattering, Australian Nuclear Science and Technology Organisation, Lucas Heights, NSW 2234, Australia
[3] School of Chemistry, The University of Sydney, Sydney, NSW 2006, Australia

E-mail: resta.susilo@hotmail.com

Received 13 October 2016, revised 8 December 2016
Accepted for publication 9 December 2016
Published 7 February 2017

Abstract

We have investigated the low temperature magnetic properties of $Dy_2Fe_2Si_2C$ by using magnetisation, specific heat, x-ray diffraction, neutron powder diffraction and ^{57}Fe Mössbauer spectroscopy measurements over the temperature range 1.5 K–300 K. $Dy_2Fe_2Si_2C$ exhibits two magnetic transitions at low temperatures: an antiferromagnetic transition at $T_N \sim 26$ K and a spin-reorientation transition at $T_t \sim 6$ K. The magnetic structure above T_t can be described with a propagation vector $\mathbf{k} = (0\,0\,\frac{1}{2})$ with the ordering of the Dy magnetic moments along the monoclinic *b*-axis whereas on cooling below T_t the Dy moment tips away from the *b*-axis towards the *ac*-plane. We find that the spin-reorientation in $Dy_2Fe_2Si_2C$ is mainly driven by the competition between the second-order crystal field term B_{20} and the higher-order terms, in particular B_{40} and B_{64}.

Keywords: neutron diffraction, magnetic structure, Mössbauer spectroscopy, rare-earth intermetallic

(Some figures may appear in colour only in the online journal)

1. Introduction

The $R_2Fe_2Si_2C$ (R = rare-earths) series of compounds was discovered by Paccard and Paccard during the attempt to synthesise a new permanent magnet [1]. These quaternary compounds crystallise in the monoclinic $Dy_2Fe_2Si_2C$-type structure with the $C2/m$ (#12) space group and form an extensive family with R = Y, La–Nd, Sm, Gd–Tm and Lu [1–3]. The R, Fe and Si atoms occupy 4i sites with *m* point symmetry and four atomic positions: $(x, 0, z)$, $(x + \frac{1}{2}, \frac{1}{2}, z)$, $(-x, 0, -z)$ and $(-x + \frac{1}{2}, \frac{1}{2}, -z)$ while the C atom occupies the 2*a* site at (0, 0, 0) and $(\frac{1}{2}, \frac{1}{2}, 0)$ with 2/*m* point symmetry. Besides this series of compounds (with Fe as the transition metal element), the isostructural $R_2Re_2Si_2C$ compounds have also been synthesised and studied [3–5].

The first magnetic studies of the $R_2Fe_2Si_2C$ (R = Y, Pr, Nd, Gd, Tb, Dy, Ho and Er) compounds by Schmitt *et al* [6] revealed that most of the compounds are antiferromagnetic, with Néel temperatures (T_N) ranging from $T_N \sim 45$ K for $Tb_2Fe_2Si_2C$ to $T_N \sim 5$ K for $Er_2Fe_2Si_2C$, whereas no magnetic order was observed for $Y_2Fe_2Si_2C$ and $Pr_2Fe_2Si_2C$ down to 2 K. The magnetic characterisations of $Tm_2Fe_2Si_2C$ and $Lu_2Fe_2Si_2C$ were reported later by Pöttgen *et al* [2] using magnetisation and resistivity measurements. They found that $Tm_2Fe_2Si_2C$ orders at $T_N = 2.7(2)$ K, while $Lu_2Fe_2Si_2C$ is non-magnetic. Based on magnetisation studies, the magnetism of the $R_2Fe_2Si_2C$ (R = Nd, Gd, Tb, Dy, Ho, Er and Tm) compounds was attributed solely to the R atoms, i.e. the Fe atom was reported to be non-magnetic as indicated by the similarity between the values of the experimental effective moment and the theoretical effective moment for the R^{3+} ions.

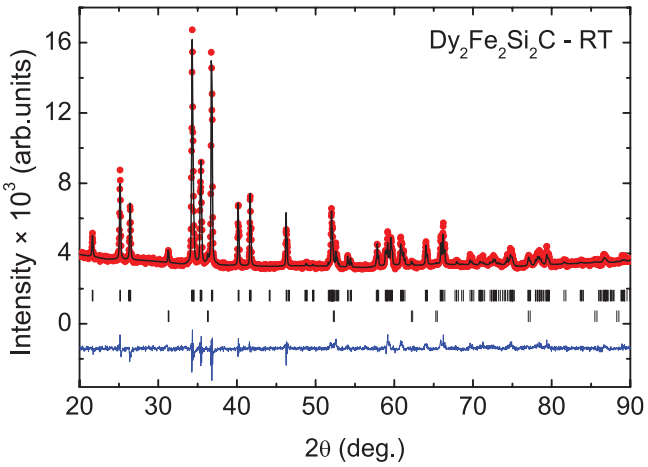

Figure 1. X-ray diffraction pattern of $Dy_2Fe_2Si_2C$ collected at room temperature (Cu–K_α radiation). Bragg markers from top to bottom represent $Dy_2Fe_2Si_2C$ and $DyC_{0.33}$, respectively. The difference between the experimental and calculated patterns is given by the blue line.

Neutron diffraction determinations of the magnetic structures of $Nd_2Fe_2Si_2C$ and $Tb_2Fe_2Si_2C$ have been reported by Le Roy *et al* [7] who proposed a doubled antiferromagnetic structure along the *c*-axis ($\mathbf{k} = (0\,0\,\frac{1}{2})$) with both the R and Fe sublattices being magnetically ordered, almost perpendicular to each other. Recent neutron diffraction studies on $Gd_2Fe_2Si_2C$, $Tb_2Fe_2Si_2C$ and $Ho_2Fe_2Si_2C$ reveal that the R sublattices order antiferromagnetically with the moments along the *b*-axis and a propagation vector $\mathbf{k} = (0\,0\,\frac{1}{2})$. Based on ^{57}Fe Mössbauer spectroscopy measurements, the Fe atom was found to be non-magnetic in these compounds [8–10]. In addition, we observed a large spontaneous magnetostriction in $Tb_2Fe_2Si_2C$ below the antiferromagnetic transition [10] which suggests the existence of a correlation between the lattice and the ordered moment in the $R_2Fe_2Si_2C$ series.

Despite the extensive magnetic characterisations on the $R_2Fe_2Si_2C$ compounds, the low temperature behaviour of $Dy_2Fe_2Si_2C$ remains unclear. Schmitt *et al* [6] reported that this compound orders antiferromagnetically below $T_N = 29$ K, however, the magnetic properties of $Dy_2Fe_2Si_2C$ were only briefly discussed without showing any magnetisation curves. In this paper, we present our investigation on the low temperature magnetic properties of $Dy_2Fe_2Si_2C$ using x-ray diffraction, magnetisation, specific heat measurements, neutron powder diffraction and ^{57}Fe Mössbauer spectroscopy. We found that, in contrast to other $R_2Fe_2Si_2C$ compounds, $Dy_2Fe_2Si_2C$ undergoes two successive magnetic transitions at low temperatures. The first transition at 26(2) K corresponds to the development of antiferromagnetic order, and our neutron diffraction and ^{57}Fe Mössbauer spectroscopy studies reveal that the second magnetic transition is likely related to a spin-reorientation of the Dy moments rather than the independent ordering of the Fe sublattice. A possible explanation of this unique occurrence in the $R_2Fe_2Si_2C$ series will be presented with particular emphasis directed towards a comparison with the isostructural $Tb_2Fe_2Si_2C$ compound.

Table 1. Crystallographic data for $Dy_2Fe_2Si_2C$ ($C2/m$ space group) as determined by x-ray powder diffraction at room temperature.

Atom	*x*	*y*	*z*
Dy	0.5622(11)	0	0.295(2)
Fe	0.201(2)	0	0.096(5)
Si	0.151(4)	0	0.694(6)
C	0	0	0
$a = 10.589(13)$ Å	$b = 3.9207(5)$ Å	$c = 6.7356(9)$ Å	$\beta = 129.25(1)°$
	$R_{Bragg}(\%) = 16.7$	$R_F(\%) = 16.4$	

2. Experimental methods

The $Dy_2Fe_2Si_2C$ samples were prepared by arc-melting the high purity elements (at least 99.9 wt%) under an argon atmosphere. The ingots were turned and re-melted several times to ensure homogeneity. X-ray powder diffraction (XRD) patterns were collected at room temperature using a PANalytical empyrean diffractometer (Cu–K_α radiation).

Magnetisation and zero field specific heat data were measured using a quantum design physical property measurement system (PPMS). Magnetisation data were collected in the temperature range between 2 K–300 K in an applied field of 1 T, while the specific heat measurements were performed in a zero field by a relaxation method between 2 K–300 K.

Neutron diffraction experiments were carried out on the Echidna high resolution powder diffractometer [11] at the OPAL reactor in Sydney, Australia with an incident neutron wavelength of 2.4395(5) Å (using the (3 3 1) reflection of a Ge monochromator). Due to the high neutron absorption associated with the Dy in $Dy_2Fe_2Si_2C$, approximately 2 g of the $Dy_2Fe_2Si_2C$ powder sample was mounted in a double-walled (annular) vanadium can to reduce the absorption effect. All neutron diffraction patterns were corrected for absorption effects and refined by the Rietveld method using the FullProf/Winplotr software [12, 13].

^{57}Fe Mössbauer spectra were collected in standard transmission mode using a ^{57}Co–**Rh** source. The spectrometer was calibrated with an α-Fe foil at room temperature and the sample temperature was varied from 5 K to 30 K using a liquid helium cryostat. All spectra were fitted using the Recoil software [14].

3. Results and discussion

3.1. Crystal structure

Refinement of the x-ray diffraction pattern collected at room temperature confirms the formation of the monoclinic $Dy_2Fe_2Si_2C$-type structure with an impurity phase, identified as $DyC_{0.33}$ (dysprosium carbide) present at a level of less than 3 wt%. The refined pattern is shown in figure 1. The crystallographic parameters of $Dy_2Fe_2Si_2C$ obtained from this refinement are presented in table 1.

3.2. Magnetic properties

In figure 2(a), we present the dc (molar) magnetic susceptibility of $Dy_2Fe_2Si_2C$ obtained with an applied field of 1 T. In

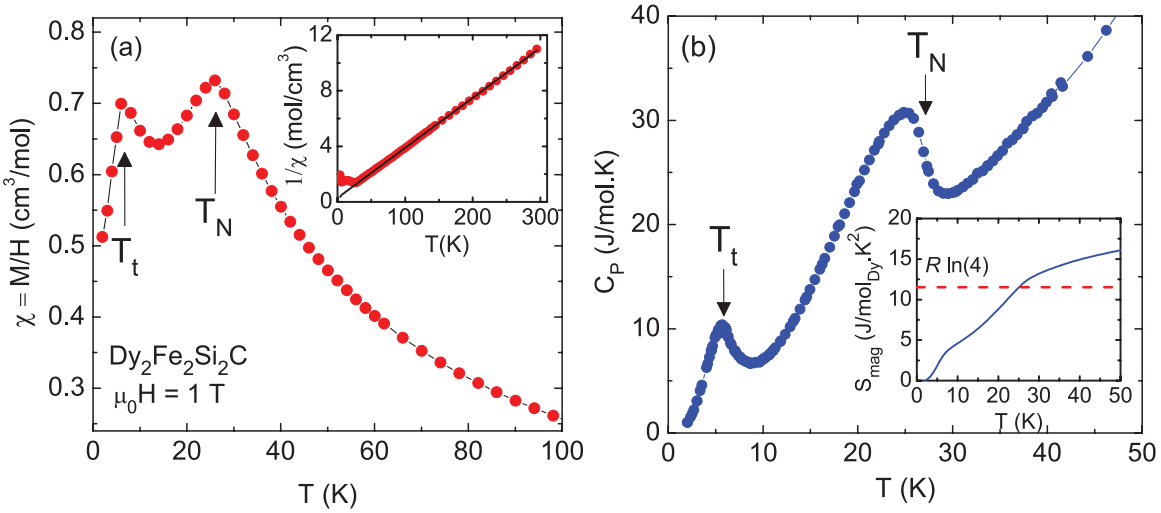

Figure 2. (a) DC susceptibility of $Dy_2Fe_2Si_2C$ obtained in field-cooled (FC) mode with an applied field of 1 T. The inset shows the inverse susceptibility and its fit to the Curie–Weiss law. (b) Zero field specific heat of $Dy_2Fe_2Si_2C$. The inset shows the calculated magnetic entropy for $Dy_2Fe_2Si_2C$.

contrast with other $R_2Fe_2Si_2C$ compounds, $Dy_2Fe_2Si_2C$ shows two magnetic transitions at low temperatures. This result is unexpected, since previous magnetic studies by Schmitt *et al* [6] showed that this compound orders at around 29 K with no second magnetic transition at lower temperature mentioned. The primary magnetic transition at $T_N = 26(2)$ K is in agreement with the previous report [6], while the second magnetic transition occurs at $T_t = 6(1)$ K. The second magnetic transition cannot be attributed to the magnetic ordering of the impurity phase, given that $DyC_{0.33}$ (impurity phase in this sample) was reported to order ferromagnetically below $T_C = 216$ K [15]. It is interesting to note that two magnetic transitions are also observed in isostructural $Dy_2Re_2Si_2C$ [5]. The Curie–Weiss fit to the inverse molar susceptibility (inset in figure 2(a)), yields a paramagnetic Curie temperature of $\theta_P = -8(1)$ K and an effective magnetic moment of $\mu_{eff} = 10.54(4)\,\mu_B$, which agrees well with the theoretical μ_{eff} of 10.64 μ_B expected for the Dy^{3+} ion. This observation indicates that the Fe magnetic moment does not contribute to the overall magnetic properties of $Dy_2Fe_2Si_2C$.

In figure 2(b), we present the low temperature specific heat data of $Dy_2Fe_2Si_2C$. Two anomalies in the specific heat are clearly observable at 26(2) K and 6(1) K, consistent with the magnetic transitions observed in the magnetisation measurements. The magnetic contribution to the entropy, S_{mag}, of $Dy_2Fe_2Si_2C$ (calculated by integrating the magnetic contribution to the specific heat) is shown in the inset of figure 2(b). The magnetic entropy released at T_N is ~11.9 J mol^{-1} K^{-1} close to $R\ln(4) = 11.53$ J mol^{-1} K^{-1} which implies two ground state doublets isolated from other levels (Dy^{3+} is a Kramers ion).

In order to get a better understanding of the low temperature magnetic behaviour of $Dy_2Fe_2Si_2C$, we carried out isothermal magnetisation measurements $M(\mu_0 H)$ at 40 K (above

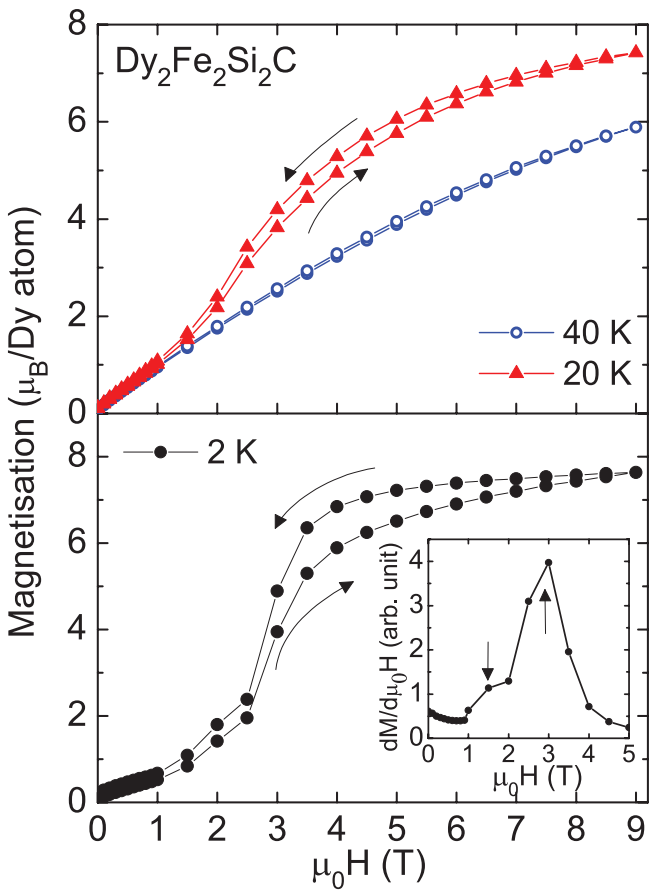

Figure 3. Isothermal magnetisation of $Dy_2Fe_2Si_2C$ measured at 40 K (above T_N; top panel) and 20 K ($T_t < T < T_N$; top panel) and at 2 K (below T_t; bottom panel). Arrows indicate the $M(\mu_0 H)$ curves measured in the increasing and decreasing fields. The inset shows the derivative $dM/d(\mu_0 H)$ at 2 K with the arrows indicating the critical fields associated with the metamagnetic transition.

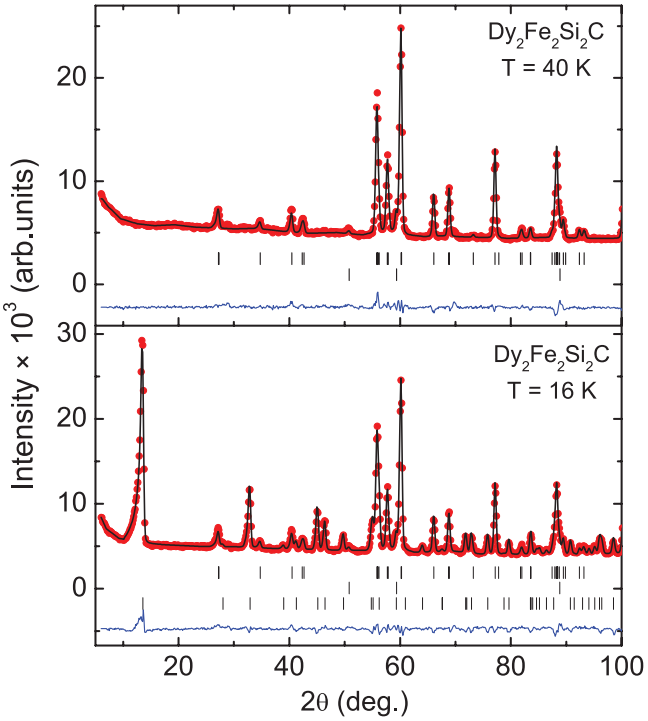

Figure 4. Rietveld refinement of the neutron diffraction patterns of $Dy_2Fe_2Si_2C$ collected at 40 K (top) and 16 K (bottom). The rows of Bragg markers, from top to bottom, represent $Dy_2Fe_2Si_2C$ (nuclear), $DyC_{0.33}$ and $Dy_2Fe_2Si_2C$ (magnetic), respectively. The difference between the experimental and calculated patterns is given by the blue line.

$T_N = 26(2)$ K), 20 K ($T_t < T < T_N$) and 2 K (below $T_t = 6(1)$ K) as shown in figure 3. The $M(\mu_0 H)$ curve obtained at 40 K shows a paramagnetic response whereas the magnetisation curve at 20 K exhibits antiferromagnetic-like behaviour with a linear increase up to $\mu_0 H = 2$ T. The magnetisation curve then undergoes a steep rise in a field larger than 2 T which can be associated with a field-induced metamagnetic transition from an antiferromagnetic state to a ferromagnetic state. The critical field associated with this metamagnetic transition is ~2 T at $T = 20$ K (determined from the maximum in $dM/d\mu_0 H$ curve). A small magnetic hysteresis is also observed at this temperature as indicated by the difference between the increasing and decreasing fields of the $M(\mu_0 H)$ curve.

The $M(\mu_0 H)$ curve obtained at 2 K (below the second magnetic transition at $T_t = 6(1)$ K) shows a more complex behaviour which we interpret as a two-step metamagnetic transition. The first metamagnetic transition occurs between 1 T and 3 T while the second transition occurs around 3 T. These two transitions are indicated by the pronounced maximum in $dM/d\mu_0 H$ at 3 T and a weaker maximum at 1.5 T (see inset in the lower panel of figure 3). In addition, an increased magnetic hysteresis is observed for fields above ~3 T. We note that a two-step metamagnetic transition was also observed in the isostructural $Dy_2Re_2Si_2C$ [5].

3.3. Neutron diffraction

Both the dc susceptibility and specific heat measurements reveal that $Dy_2Fe_2Si_2C$ undergoes two successive magnetic transitions at $T_N = 26(2)$ K and at $T_t = 6(1)$ K. In order to determine the magnetic structure and to study the nature of the second magnetic transition, we have performed neutron diffraction experiments. Neutron diffraction patterns of $Dy_2Fe_2Si_2C$ taken at 40 K and 16 K are shown in figure 4. The pattern collected at 40 K, above $T_N = 26(2)$ K, represents the nuclear scattering from the monoclinic $C2/m$ cell. The refinement parameters for the 40 K pattern are summarised in table 2.

The diffraction pattern obtained at 16 K shows several magnetic peaks, with dominant contributions occurring at $2\theta \sim 13°, 33°, 45°$ and 46°, respectively. These magnetic peaks can be indexed with a propagation vector $\mathbf{k} = (0, 0, \frac{1}{2})$. In order to determine all possible allowed magnetic structures for the Dy atom at the 4i site, we carried out representational analysis using the BasIReps program, part of the Fullprof/WinPlotr suite [12, 13]. The decomposition of the magnetic representation comprises four one-dimensional representations, with two of them appearing twice:

$$\Gamma^{4i} = 1\Gamma_1 + 2\Gamma_2 + 2\Gamma_3 + \Gamma_4. \quad (1)$$

The basis vectors of these irreducible representations are given in table 3. It should be noted that due to the identical point symmetries of the Dy and Fe atoms (both occupy 4i sites), these irreducible representations are also applicable to the Fe atom.

The best refinement to the diffraction pattern at 16 K is obtained using the Γ_4 representation with the ordering of the Dy magnetic moment along the b-axis, similar to the cases of $Gd_2Fe_2Si_2C$ [9], $Tb_2Fe_2Si_2C$ [10] and $Ho_2Fe_2Si_2C$ [8]. The refined Dy moment at 16 K is 6.6(1) μ_B with the refinement parameters for the 16 K pattern shown in table 2.

A comparison of the patterns taken at 16 K and 1.5 K, above and below $T_t \sim 6$ K is presented in figure 5. Upon cooling below $T_t \sim 6$ K, we observe the appearance of the (0 2 0) magnetic peak at $2\theta \sim 79°$ that was absent in the diffraction pattern taken at 16 K. Similar changes in intensity also occur at other magnetic peaks, suggesting a change in magnetic structure. We consider it likely that the appearance of the (0 2 0) magnetic peak indicates a spin-reorientation of the Dy magnetic moment away from the b-axis, however the possibility of independent ordering of the Fe sublattice below T_t cannot be ruled out at this stage. We note that the (0 2 0) magnetic peak will also appear if the Fe moment orders independently in the ac-plane, with the Dy magnetic moment still aligned along the b-axis.

In order to determine the magnetic structure of $Dy_2Fe_2Si_2C$ below $T_t \sim 6$ K, two different refinement models were employed. First, we carried out refinement of the 1.5 K pattern by allowing the x- and z-components of the Dy magnetic moment to vary (model A). The 1.5 K pattern can be fitted well with a canted magnetic structure of the Dy magnetic moment corresponding to a combination of Γ_2 and Γ_4 representations. The refined Dy moment is 9.6(2) μ_B which is essentially the free-ion value of 10 μ_B. The refinement parameters of the 1.5 K pattern using a canted magnetic structure are given in table 2.

Table 2. Crystallographic and magnetic parameters of $Dy_2Fe_2Si_2C$ derived from the refinement of the neutron diffraction patterns obtained at 40 K, 16 K and 1.5 K. The different models applied in the refinements are discussed in the text.

	40 K	16 K	1.5 K (model A)	1.5 K (model B)
x_{Dy}	0.5616(7)	0.5612(7)	0.5603(9)	0.5601(9)
z_{Dy}	0.292(1)	0.293(1)	0.292(1)	0.291(2)
x_{Fe}	0.202(1)	0.203(2)	0.200(2)	0.200(2)
z_{Fe}	0.094(2)	0.095(3)	0.090(3)	0.090(3)
x_{Si}	0.167(3)	0.166(3)	0.167(5)	0.167(5)
z_{Si}	0.719(6)	0.719(5)	0.710(6)	0.710(6)
a (Å)	10.5712(4)	10.5744(5)	10.5734(6)	10.5731(6)
b (Å)	3.9154(2)	3.9145(2)	3.9145(3)	3.9145(3)
c (Å)	6.7175(3)	6.7197(3)	6.7202(5)	6.7202(5)
β (°)	129.25(1)	129.27(1)	129.26(1)	129.26(1)
μ_x^{Dy} (μ_B)	—	—	4.2(6)	—
μ_y^{Dy} (μ_B)	—	6.6(1)	8.8(2)	9.1(2)
μ_z^{Dy} (μ_B)	—	—	5.0(4)	—
μ_x^{Fe} (μ_B)	—	—	—	3.1(9)
$\mu_{y^{Fe}}$ (μ_B)	—	—	—	—
μ_z^{Fe} (μ_B)	—	—	—	4.3(7)
μ_{Dy} (μ_B)	—	6.6(1)	9.6(2)	9.1(2)
μ_{Fe} (μ_B)	—	—	—	3.3(2)
R_p (%); R_{wp} (%)	13.4; 9.8	11.4; 9.5	14.5; 12.7	15.1; 13.5
R_{Bragg} (%); R_F (%)	4.3; 2.9	4.8; 3.2	9.2; 5.8	9.2; 5.8
R_{mag}	—	6.0	9.4	11.5 (Dy); 14.5 (Fe)

Table 3. Representational analysis for the Dy and Fe atoms at the 4i site in $Dy_2Fe_2Si_2C$ with a propagation vector $\mathbf{k} = (0\,0\,\frac{1}{2})$.

Atomic positions	Γ_1	Γ_2	Γ_3	Γ_4
$(x, 0, z)$	(0 v 0)	(u 0 w)	(u 0 w)	(0 v 0)
$(x + 1/2, 1/2, z)$	(0 v 0)	(u 0 w)	(u 0 w)	(0 v 0)
$(-x, 0, -z)$	(0 v 0)	(−u 0 −w)	(u 0 w)	(0 −v 0)
$(-x + 1/2, 1/2, -z)$	(0 v 0)	(−u 0 −w)	(u 0 w)	(0 −v 0)

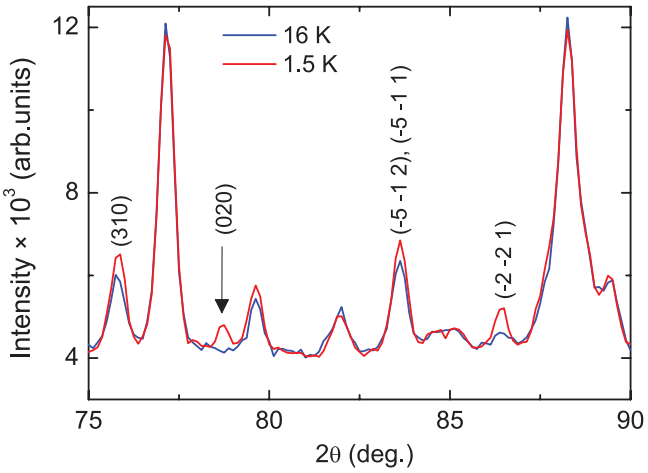

Figure 5. Comparison of neutron powder diffraction patterns of $Dy_2Fe_2Si_2C$ collected at 16 K and 1.5 K with a neutron wavelength of 2.4395(5) Å.

The second model (model B) involves ordering of both the Dy and Fe moments. For this refinement model, the direction of the Dy moment was constrained along the *b*-axis, while all three components of the Fe magnetic moment were allowed to vary. We found that the 1.5 K pattern can also be fitted using the *b*-axis order of the Dy magnetic moment and the Fe magnetic moment in the *ac*-plane, with the refinement parameters of the 1.5 K pattern summarised in table 2. The refined Dy and Fe moments for model B at 1.5 K are 9.1(2) μ_B and 3.3(2) μ_B, respectively.

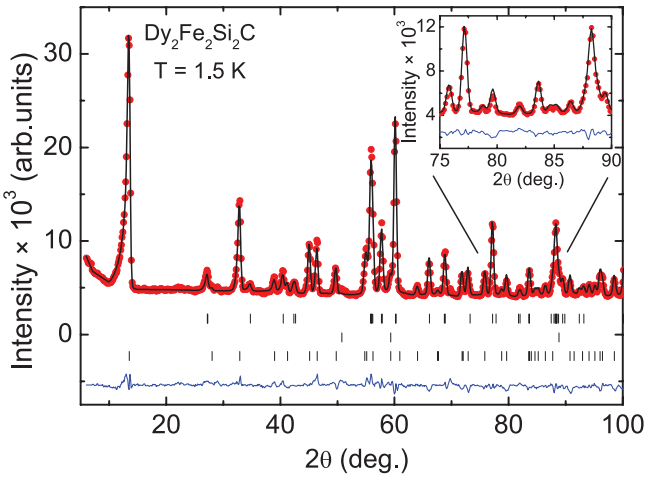

Figure 6. Rietveld refinement of the neutron diffraction pattern of $Dy_2Fe_2Si_2C$ collected at 1.5 K. The rows of Bragg markers, from top to bottom, represent $Dy_2Fe_2Si_2C$ (nuclear), $DyC_{0.33}$ and $Dy_2Fe_2Si_2C$ (magnetic), respectively. The difference between the experimental and calculated patterns is given by the blue line. The inset shows a representative portion of the refined pattern in the 2θ range of 75° to 90°.

It can be seen in table 2 that the second model yields higher magnetic *R*-factors compared to the first model (without an Fe moment). Moreover, the refined Fe moment of 3.3 μ_B is too large for a metallic Fe moment. Therefore, we conclude that

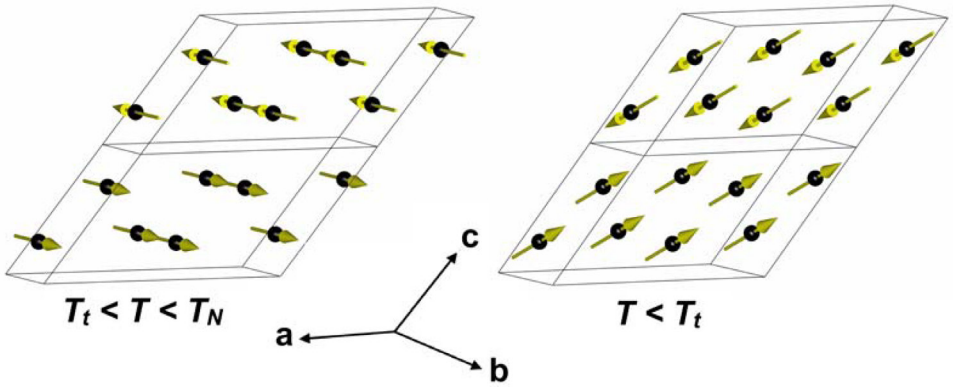

Figure 7. Magnetic structures of $Dy_2Fe_2Si_2C$ above and below the spin-reorientation transition T_t. Each block corresponds to a nuclear unit cell. The Fe, Si and C atoms are omitted for clarity.

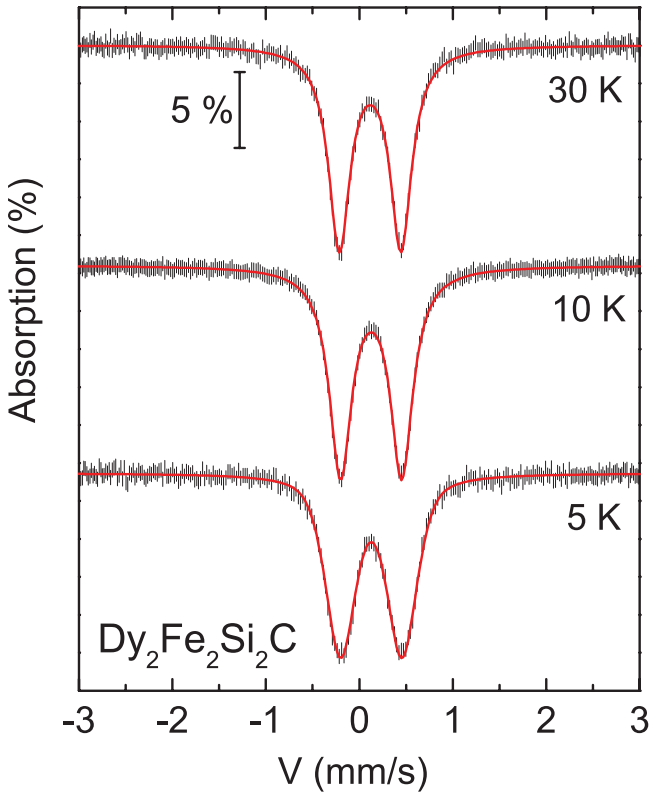

Figure 8. ^{57}Fe Mössbauer spectra of $Dy_2Fe_2Si_2C$ collected at 30 K (above $T_N = 26(2)$ K), 10 K (below T_N) and 5 K (below $T_t = 6(1)$ K).

the second magnetic transition observed at 6 K in the magnetisation and specific heat data is related to a spin-reorientation transition of the Dy magnetic moment rather than the ordering of the Fe sublattice. In figure 6, we show the refinement for the 1.5 K pattern using a canted magnetic structure of the Dy magnetic moment i.e. model A. The resultant magnetic structures of $Dy_2Fe_2Si_2C$ above and below the spin-reorientation transition T_t are shown in figure 7.

3.4. ^{57}Fe Mössbauer spectroscopy

^{57}Fe Mössbauer spectra of $Dy_2Fe_2Si_2C$ collected at 30 K (above $T_N = 26(2)$ K), at 10 K (below $T_N = 26(2)$ K) and 5 K (below $T_t \sim 6$ K) are presented in figure 8. The spectrum at 30 K shows only a quadrupole doublet and can be fitted with a quadrupole splitting of $QS = 0.658(3)$ mm s^{-1} and an isomer shift of $IS = 0.126(2)$ mm s^{-1}. Similar to the cases of $Gd_2Fe_2Si_2C$ [9], $Tb_2Fe_2Si_2C$ [10] and $Ho_2Fe_2Si_2C$ [8], we observed no magnetic splitting down to 5 K, indicating that the Fe atom is non-magnetic. This result also confirms our earlier conclusion from neutron diffraction refinements that the second magnetic transition at $T_t = 6(1)$ K is in fact related to a spin-reorientation of the Dy moment and is not associated with the independent ordering of the Fe sublattice. The temperature dependences of the hyperfine parameters are shown in figure 9.

A slight line broadening of $\sim$0.01 mm s^{-1} is observed in the spectra collected below $T_N = 26(2)$ K down to 10 K (top panel of figure 9); this broadening can be attributed to a small transferred hyperfine field at the Fe site due to the ordering of the Dy sublattice. On cooling below 10 K we observed a significant line broadening of $\sim$0.05 mm s^{-1} from FWHM = 0.29(3) mm s^{-1} (at 10 K) to FWHM = 0.343(6) mm s^{-1} (at 5 K). This significant line broadening in the ^{57}Fe Mössbauer spectrum occurs around the spin-reorientation transition of this compound ($T_t = 6(1)$ K), and therefore can be attributed to the increase of the transferred hyperfine field at the Fe site due to a change in the orientation of the Dy magnetic moments. We note that the temperature dependence of transferred hyperfine field is commonly found to undergo an inflection below the spin-reorientation transition (see for example the temperature dependence of transferred hyperfine field at the Sn site in $Tb_3Ag_4Sn_4$ [16] and $Gd_3Ag_4Sn_4$ [17]). Interestingly, the temperature dependence of the quadrupole splitting and the isomer shift remain constant (within the uncertainties) from 30 K to 5 K.

3.5. Crystal field analysis and magnetocrystalline anisotropy energy calculation

The spin-reorientation observed in $Dy_2Fe_2Si_2C$ is unique compared with other $R_2Fe_2Si_2C$ compounds. In the $R_2Fe_2Si_2C$ (R = Gd, Tb and Ho) compounds, the magnetic structure is characterised by a cell-doubling along the c-axis ($\mathbf{k} = (0\,0\,\frac{1}{2})$) with the R magnetic moment pointing along the b-direction. The magnetic structure of $Dy_2Fe_2Si_2C$ is

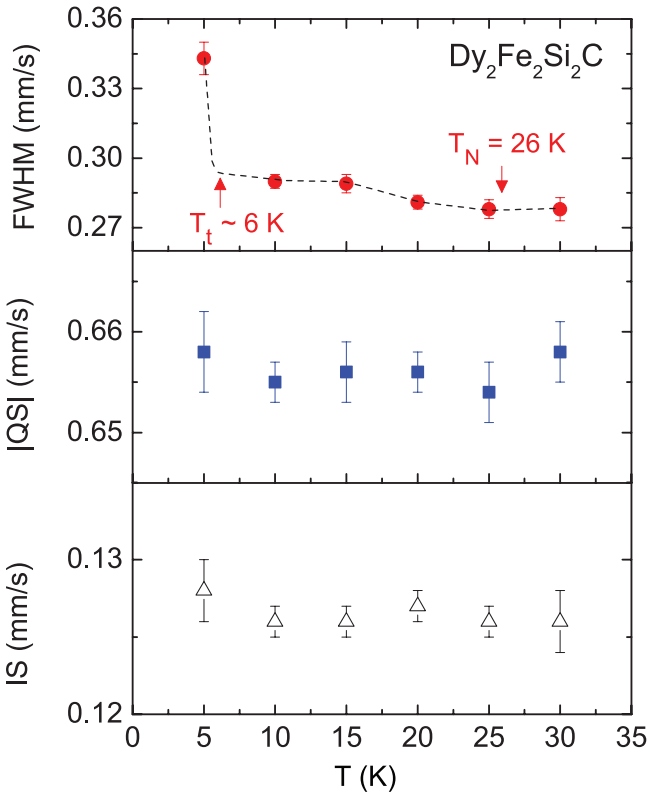

Figure 9. Temperature dependences of the hyperfine parameters of $Dy_2Fe_2Si_2C$. The dashed lines are visual guides. FWHM, QS and IS represent the linewidth, quadrupole splitting and isomer shift, respectively.

similarly characterised by a cell-doubling along the *c*-axis with $\mathbf{k} = (0\,0\,\frac{1}{2})$ although the Dy magnetic moment is canted away from the *b*-axis towards the *ac*-plane on cooling below the spin-reorientation transition T_t.

The observation of spin-reorientation is not uncommon in rare-earth transition metal compounds where the transition metal sublattice is magnetically ordered such as in the case of the $RFe_{11}Ti$ [18] and the RMn_6Sn_6 [19] systems. In such systems, the spin-reorientation occurs due to the competition between the magnetic anisotropy of the transition metal and rare-earth sublattices. Such a scenario, however, cannot be expected in the $R_2Fe_2Si_2C$ series where the Fe sublattice is non-magnetic which suggests that crystal field effects are responsible for the spin-reorientation process. In $Tb_2Fe_2Si_2C$ and $Ho_2Fe_2Si_2C$, the R magnetic moment is aligned along the *b*-axis and no spin-reorientation is observed down to 3 K [8, 10]. Given that the Tb^{3+}, Dy^{3+} and Ho^{3+} ions have a negative second-order Stevens coefficient [20], the direction of the Dy magnetic moment in $Dy_2Fe_2Si_2C$ is not dictated by the second-order crystal field term, and the occurrence of a spin-reorientation in this compound—in contrast to $Tb_2Fe_2Si_2C$ and $Ho_2Fe_2Si_2C$—is likely to be driven by the competition between the second-, fourth- and sixth-order crystal field terms acting on the Dy^{3+} ion. In table 4, we show the signs of the Stevens coefficients appropriate for the Tb^{3+}, Dy^{3+} and Ho^{3+} ions.

In $R_2Fe_2Si_2C$, the R^{3+} ion occupies the 4i site with monoclinic *m* symmetry. If the *z*-axis of the Stevens operators is

Table 4. Signs of the Stevens coefficients (second-order α_J, fourth-order β_J and sixth-order γ_J) for the Tb^{3+}, Dy^{3+} and Ho^{3+} ions [20].

R	α_J	β_J	γ_J
Tb^{3+}	−	+	+
Dy^{3+}	−	−	+
Ho^{3+}	−	−	−

taken along the two-fold symmetry axis i.e. the crystal *b*-axis in the *C*2/*m* space group, the crystal field Hamiltonian for the monoclinic symmetry is given by (e.g. [21])

$$\begin{aligned} H_{CF} = {} & B_{20}O_{20} + B^c_{22}O^c_{22} + B^s_{22}O^s_{22} + B_{40}O_{40} + B^c_{42}O^c_{42} \\ & + B^c_{44}O^c_{44} + B^s_{42}O^s_{42} + B^s_{44}O^s_{44} + B_{60}O_{60} + B^c_{62}O^c_{62} \\ & + B^c_{64}O^c_{64} + B^c_{66}O^c_{66} + B^s_{62}O^s_{62} + B^s_{64}O^s_{64} + B^s_{66}O^s_{66} \end{aligned} \tag{2}$$

where the B_{nm} are the crystal field parameters and O_{nm} are the Stevens operators [20]. In order to simplify our crystal field analysis, we adopted approach (A) outlined by Rudowicz in [21], in which only the real components of the crystal field parameters are considered, thereby reducing the Hamiltonian to an orthorhombic approximation of the monoclinic symmetry. Consequently, the total number of crystal field parameters is reduced from fifteen to nine. Within this approximation, the magnetic anisotropy energy of the R^{3+} sublattice up to fourth-order in angle can be written as [22, 23]

$$\begin{aligned} E_{an} = {} & -\frac{3}{2}B_{20}\langle O_{20}\rangle \sin^2\theta + B_{40}\langle O_{40}\rangle\left[-5\sin^2\theta + \frac{35}{8}\sin^4\theta\right] \\ & + B_{60}\langle O_{60}\rangle\left[-\frac{21}{2}\sin^2\theta + \frac{189}{8}\sin^4\theta\right] \\ & + B^c_{22}\langle O_{20}\rangle\left[\frac{1}{2}\sin^2\theta\cos 2\phi\right] \\ & + B^c_{42}\langle O_{40}\rangle\left[\frac{3}{4}\sin^4\theta\cos 4\phi - \frac{7}{8}\sin^4\theta\cos 2\phi\right] \\ & + B^c_{44}\langle O_{40}\rangle\left[\frac{1}{8}\sin^4\theta\cos 4\phi\right] \\ & + B^c_{62}\langle O_{60}\rangle\left[\frac{3}{4}\sin^2\theta\cos 2\phi + \frac{21}{8}\sin^4\theta\cos 2\phi\right] \\ & + B^c_{64}\langle O_{60}\rangle\left[\frac{5}{8}\sin^4\theta\cos 4\phi\right] \end{aligned} \tag{3}$$

where θ and ϕ are the polar and azimuth angles of the magnetisation direction relative to the crystal *b*-axis, respectively. We also note that within the orthorhombic approximation of the monoclinic symmetry and under the assumption that the monoclinic *b*-axis is the quantisation axis, the *x*- and *y*-axes of the crystal field Hamiltonian must lie in the monoclinic *ac*-plane (perpendicular to the quantisation axis, i.e. perpendicular to the monoclinic *b*-axis).

Given that the crystal field parameters B_{nm} are directly proportional to the crystal field coefficients A_{nm} i.e. $B_{nm} = A_{nm}\langle r^n\rangle\theta_n$ (where $\langle r^n\rangle$ are the 4f radial expectation values and θ_n are the Stevens coefficients [20]), and under the assumption that the crystal field coefficients are constant

Table 5. Crystal field coefficients for the R^{3+} ion in $R_2Fe_2Si_2C$. Experimental values are deduced from ^{155}Gd Mössbauer studies on $Gd_2Fe_2Si_2C$ at 5 K [9] whereas the calculated values are obtained from point-charge calculations as discussed in the text.

	Exp	Calc
A_{20} (K a_0^{-2})	349.7	349.1
A_{22}^c (K a_0^{-2})	349.7	343.7
A_{40} (K a_0^{-4})		−44.0
A_{42}^c (K a_0^{-4})		159.0
A_{44}^c (K a_0^{-4})		238.1
A_{60} (K a_0^{-6})		0.1
A_{62}^c (K a_0^{-6})		−1.9
A_{64}^c (K a_0^{-6})		5.5
A_{66}^c (K a_0^{-6})		−0.3

across the $R_2Fe_2Si_2C$ series, the first step that needs to be done is to estimate the crystal field coefficients A_{nm}. For initial analysis, we estimated the second-order crystal field coefficients A_{20} and A_{22}^c from previous ^{155}Gd Mössbauer measurements on $Gd_2Fe_2Si_2C$ [9]. For the 4f electrons, there are two contributions to the total electric field gradient (EFG) at the R nucleus, namely the 4f electron shell and the surrounding lattice charges. The latter contribution is assumed to be directly proportional to the second-order crystal field coefficient A_{20}. In the case of an S-state ion such as a Gd^{3+} ion, the contribution of the 4f shell to the total EFG is zero, leaving the EFG contribution from the surrounding lattice charges. In such cases, the lattice contribution to the EFG can be written as

$$V_{ZZ} = -\frac{4A_{20}(1-\gamma_\infty)_{Gd}}{|e|} \tag{4}$$

where V_{ZZ} is the principal component of the EFG tensor, γ_∞ is the Sternheimer antishielding factor and $|e|$ is the fundamental electronic charge. At the same time, the off-diagonal second-order crystal field coefficient A_{22}^c can be estimated from the asymmetry parameter η of the ^{155}Gd Mössbauer spectrum via

$$\eta = \frac{A_{22}^c}{A_{20}}. \tag{5}$$

The fit to the ^{155}Gd spectrum of $Gd_2Fe_2Si_2C$ collected at 5 K yields $eQV_{ZZ} = -1.20$ mm s^{-1} [9]. The corresponding value of V_{ZZ} is -2.67×10^{21} V m^{-2} based on the value $Q = (1.30 \pm 0.02)\,b$ for the ^{155}Gd ground state [24]. We note that for the 86.5 keV Mössbauer transition in ^{155}Gd, 1 mm s^{-1} converts to 4.625×10^{-26} J [25]. By using the value of $(1-\gamma_\infty)_{Gd} = 61.87$ appropriate for Gd^{3+} [26], we obtained $A_{20} = 349.7$ K a_0^{-2}. On the basis of the asymmetry parameter of the ^{155}Gd Mössbauer spectrum at 5 K, i.e. $\eta = 1$ [9], the off-diagonal second-order coefficient is equal to the diagonal coefficient i.e. $A_{22}^c = A_{20} = 349.7$ K a_0^{-2}.

We then used point-charge calculations out to 10 Å to estimate the higher-order terms. We realise that this model is a poor approximation especially in a metallic system, however it should give a reasonable description of the relative magnitudes

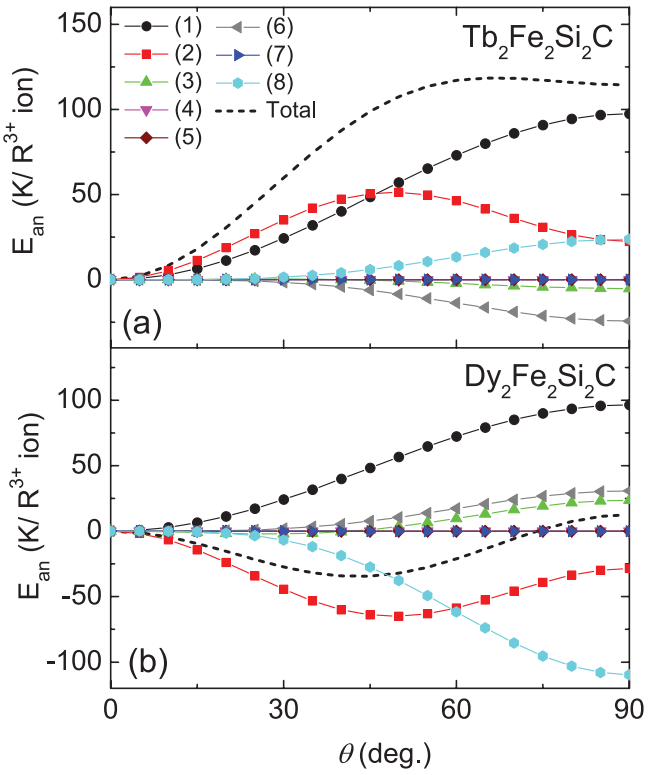

Figure 10. Calculated total magnetic anisotropy energy, together with the contributions from each crystal field term for (a) $Tb_2Fe_2Si_2C$ and (b) $Dy_2Fe_2Si_2C$ at 5 K. The contributions of the individual crystal field terms used to calculate the total magnetic anisotropy energy as in equation (3) are plotted with symbols and identified as: (1) $B_{20}\langle O_{20}\rangle$, (2) $B_{40}\langle O_{40}\rangle$, (3) $B_{60}\langle O_{60}\rangle$, (4) $B_{22}\langle O_{22}\rangle$, (5) $B_{42}\langle O_{42}\rangle$, (6) $B_{44}\langle O_{44}\rangle$, (7) $B_{62}\langle O_{62}\rangle$ and (8) $B_{64}\langle O_{64}\rangle$ terms.

of the crystal field terms. We find that by assuming effective charges of +3, +2, −2.1 and −4.3 on the R, Fe, Si and C, respectively, and by taking the crystal b-axis as the quantisation axis, we obtained a rather good agreement between the calculated and experimental A_{20} and A_{22}^c values (see table 5). The calculated values of the crystal field coefficients out to sixth order are shown in table 5. We then used these crystal field coefficients to calculate the crystal field parameters B_{nm} and calculate the magnetocrystalline anisotropy energies, including the contribution from each of the crystal field terms, for $Dy_2Fe_2Si_2C$ and $Tb_2Fe_2Si_2C$ as a function of θ, i.e. the angle of the R magnetic moment relative to the quantisation axis (the monoclinic b-axis). Given that the Dy moments form a canted magnetic structure with three magnetic components below T_t, the azimuth angle ϕ was set to non-zero. In these calculations, we fixed the azimuth angle ϕ to 45° relative to the x-axis of the crystal field Hamiltonian for both cases. The calculated total magnetocrystalline anisotropy energies for $Dy_2Fe_2Si_2C$ and $Tb_2Fe_2Si_2C$ are presented in figure 10. In order to identify the contributions of the individual crystal field parameters to the total magnetocrystalline anisotropy energy, the terms in equation (3) are also plotted as numbered symbols in figure 10.

For $Tb_2Fe_2Si_2C$, the minimum anisotropy energy occurs at $\theta = 0$ i.e. with the Tb moments aligned along the b-axis. This observation is in agreement with our neutron diffraction

studies in which we found that the Tb magnetic moment is oriented along the *b*-axis at 3 K [10]. It can also be seen that most of the crystal field parameters, in particular B_{20}, B_{40} and B_{64} contribute constructively to the total anisotropy energy and favour the *b*-axis order. In contrast, the higher-order terms in $Dy_2Fe_2Si_2C$, specifically B_{40} and B_{64}, have opposite contributions to that of B_{20} due to the negative and positive signs of the fourth- and sixth-order Stevens coefficients, respectively (see the signs of the Stevens coefficients for the Dy^{3+} ion in table 4). As a result, a canted magnetic structure is more energetically favourable in $Dy_2Fe_2Si_2C$, as indicated by the observation of a minimum anisotropy energy at $\theta \sim 40°$. It is also interesting to note that although the positive signs of B_{40} and B_{64} favour a canted magnetic structure, the Dy magnetic moment will not be fully aligned in the *ac*-plane due to the negative sign of B_{20}. Therefore, based on our calculations, we conclude that a spin-reorientation in $Dy_2Fe_2Si_2C$ occurs due to the competition between B_{20} and the higher-order terms, in particular B_{40} and B_{64}.

4. Conclusions

We have shown that $Dy_2Fe_2Si_2C$ undergoes two successive magnetic transitions, the antiferromagnetic T_N and spin-reorientation T_t transitions, at low temperatures. The magnetic structure of $Dy_2Fe_2Si_2C$ just below $T_N = 26(2)$ K is commensurate antiferromagnetic along the *b*-axis with a propagation vector $\mathbf{k} = (0\,0\,\frac{1}{2})$, whereas below $T_t = 6(1)$ K the Dy magnetic moment tips away from the *b*-axis towards the *ac*-plane. ^{57}Fe Mössbauer spectroscopy establishes that the lower-temperature magnetic transition is not related to the independent ordering of the Fe sublattice. Magnetocrystalline anisotropy energy calculations predict the *b*-axis order of the Tb magnetic moment in $Tb_2Fe_2Si_2C$, in agreement with the experimental findings, whereas a canted magnetic structure is more energetically favourable in the case of $Dy_2Fe_2Si_2C$ due to the important influence of higher-order crystal field terms at low temperatures which explains the origin of a spin-reorientation in this compound.

Acknowledgments

RAS acknowledges receipt of a University International Postgraduate Award (UIPA) from the University of New South Wales and a Research Publication Fellowship from UNSW Canberra.

References

[1] Paccard L and Paccard D 1988 *J. Less Common Met.* **136** 297–301
[2] Pöttgen R, Ebel T, Evers C B H and Jeitschko W 1995 *J. Solid State Chem.* **114** 66–72
[3] Hüfken T, Witte A M and Jeitschko W 1998 *J. Alloys Compd.* **266** 158–63
[4] Chinchure A D, Dhar S K, Nagarajan R, Marathe V R and Gupta L C 1999 *J. Magn. Magn. Mater* **195** 43–8
[5] Chinchure A D, Doerr M, Behr G, Dhar S K, Nagarajan R, Marathe V R, Loewenhaupt M and Gupta L C 2001 *Physica* B **299** 135–41
[6] Schmitt D, Paccard D and Paccard L 1992 *Solid State Commun.* **84** 357–61
[7] Le Roy J, Paccard D, Bertrand C, Soubeyroux J L, Bouillot J, Paccard L and Schmitt D 1993 *Solid State Commun.* **86** 675–8
[8] Susilo R A, Cadogan J M, Cobas R, Hutchison W D, Avdeev M and Campbell S J 2015 *J. Appl. Phys.* **117** 17C113
[9] Ryan D H, Mas N, Susilo R A, Cadogan J M and Flacau R 2015 *J. Phys.: Condens. Matter* **27** 146005
[10] Susilo R A, Cadogan J M, Hutchison W D, Avdeev M, Cobas R, Munoz-Pérez S and Campbell S J 2016 *J. Alloys Compd.* **654** 392–8
[11] Liss K D, Hunter B, Hagen M, Noakes T and Kennedy S 2006 *Physica* B **385–6** 1010–2
[12] Rodríguez-Carvajal J 1993 *Physica* B **192** 55–69
[13] Roisnel T and Rodríguez-Carvajal J 2001 *Mat. Sci. Forum* **378–81** 118–23
[14] Lagarec K and Rancourt D G 1998 *Recoil-Mössbauer Spectral Analysis Software for Windows and ver. 1.0* (Ottawa, ON: University of Ottawa)
[15] Aoki Y and Williams D 1979 *J. Less Common Met.* **65** 35–40
[16] Perry L K, Ryan D H, Canepa F, Napoletano M, Mazzone D, Riani P and Cadogan J M 2006 *J. Appl. Phys.* **99** 08J502
[17] Voyer C J, Ryan D H, Napoletano M and Riani P 2007 *J. Phys.: Condens. Matter* **19** 156209
[18] Kou X C, Zhao T S, Grössinger R, Kirchmayr H R, Li X and de Boer F R 1993 *Phys. Rev.* B **47** 3231
[19] Malaman B, Venturini G, Welter W, Sanchez J P, Vulliet P and Ressouche E 1999 *J. Magn. Magn. Mater* **202** 519–34
[20] Stevens K W H 1952 *Proc. Phys. Soc.* A **65** 209
[21] Rudowicz C 1986 *J. Chem. Phys.* **84** 5045–58
[22] Cadogan J M, Ryan D H and Swainson I P 2000 *J. Phys.: Condens. Matter* **12** 8963
[23] Wang J L, Campbell S J, Cadogan J M, Tegus O and Edge A V J 2005 *J. Phys.: Condens. Matter* **17** 3689
[24] Tanaka Y, Laubacher D, Steffen R, Shera E, Wohlfahrt H and Hoehn M 1982 *Phys. Lett.* B **108** 8–10
[25] Cadogan J M and Ryan D H 2006 *Handbook of Applied Solid State Spectroscopy* ed D Vij (Berlin: Springer) ch 5, pp 201–56
[26] Gupta R P and Sen S K 1973 *Phys. Rev.* A **7** 850–8